Dual-energy bone densitometry using a single 100 ns x-ray pulse

John F. Seely[a)]
Naval Research Laboratory, Code 7674, Washington, DC 20375-5352

Craig N. Boyer
Universities Space Research Associates, 300 D Street SW, Washington, DC 20024

Glenn E. Holland
Sachs Freeman Associates, Inc., 1401 McCormick Drive, Landover, Maryland 20785

(Received 12 March 1998; accepted for publication 20 July 1998)

A pulsed, portable hard x-ray source has been developed for medical imaging and flash x-ray absorptiometry. The source is powered by a Marx generator that drives a field emission x-ray tube which produces a 30–300 keV x-ray pulse of 100 ns duration. The x-ray fluence has dual-energy properties. The x-ray energy is relatively high early in the pulse and lower later in the pulse. The feasibility of using a single x-ray pulse for precision bone densitometry was analyzed. A computer simulation model was developed for the x-ray source, the filtration that enhances the dual-energy distribution, the absorption of the energy distribution by bone mineral and soft tissue, and the dual-energy detection system. It is feasible to determine the bone mineral density (BMD) of axial sites such as the lumbar spine and proximal femur with 2% precision over an area that is 15–20 mm in size, depending on the bone mineral and soft tissue thicknesses. An algorithm for determining the absolute BMD, to an accuracy of 2%, using a Plexiglas™/TiO_2 calibration phantom is discussed. At a distance of 50 cm from the source, the patient exposure is 3.7 mR. The average absorbed bone and tissue doses are 0.6 and 4.3 mrem, respectively. Factors that facilitate diagnostic measurements in clinical settings are the short patient observation time and the portability of the x-ray source.
 [S0094-2405(98)00810-4]

Key words: dual-energy imaging, x-ray absorptiometry, bone densitometry, bone mineral

I. INTRODUCTION

Precision bone mineral densitometry is important for the early detection of osteoporosis and the prediction of future bone fracture risk.[1] Bone mineral loss is associated with aging and is more rapid in post-menopausal women. In addition, bone mineral loss is accelerated during long-term bed rest and in the weightless environment of space.[2]

Clinical studies indicate that the association of measured bone density with osteoporosis and bone fracture is more significant for the major weight-bearing axial sites (lumbar spine and proximal femur) than for extremity sites (hand, radius, and calcaneus).[1,3–6] The bone mineral content is correlated with the vertebral strength determined *in vitro*.[7] Clinical studies indicate that the preferred site for bone mineral densitometry may be the lumbar spine (L2–L4), and the preferred view is lateral rather than anterior–posterior (AP).[4,5] The lateral view of the vertebrae is not obscured by the posterior vertebral elements. This permits the isolation of the trabecular bone region that is most susceptible to mineral loss. However, soft tissue absorption can affect lateral projection measurements to a greater extent than AP projection measurements.

It has been estimated that a measured bone mineral density (BMD) that is one standard deviation (approximately 2%) below the average for a control population implies a significantly higher risk of a future bone fracture.[1] Thus the bone densitometry technique should have at least 2% precision and absolute accuracy.

In many clinical settings, it is important to determine BMD with a short patient observation time. In addition, since BMD measurements may be repeated over a period of time, the exposure to the patient should be as low as possible for each observation. Although ultrasonic and magnetic resonance methods are convenient and have no x-ray exposure, they do not have the required accuracy at the present time.[1]

The rather high precision and accuracy required for bone densitometry resulted in the development of x-ray radiographic absorption techniques. Bone densitometry apparatus for the hand, radius, and calcaneus were developed. However, these measurements are not as significant as axial site measurements for diagnosing osteoporosis and predicting fracture risk.

Quantitative computed tomography (QCT) x-ray scanning techniques produce three-dimensional images of skeletal regions. This permits the elimination of soft tissue attenuation and the precise determination of the BMD of interior trabecular bone regions.[1] However, QCT techniques are not suitable for repeated clinical measurements because of the high patient dose (surface dose ~100 mrem), the long patient positioning and immobilization time (tens of minutes), and the relatively high cost of the apparatus.

Dual-energy x-ray absorptiometry (DEXA) projection scanning units have been developed by Hologic Inc. (Waltham, MA), Lunar Corp. (Madison, WI), and others. Using dual-energy calibration and subtraction algorithms, the attenuation by soft tissue is effectively eliminated from the

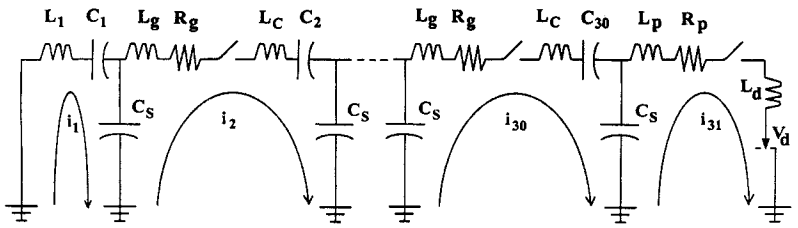

FIG. 1. Equivalent circuits for the trigger (stage 1), the Marx generator (stages 2–30), and the x-ray tube (stage 31).

measurement, and the BMD of axial sites can be precisely and accurately determined.[8–11] In the case of lumbar spine and proximal femur measurements, clinical studies indicate a typical precision of 1%–3% and an absolute accuracy of 4%–15%.[1] The patient surface dose is typically of order 10 mrem.[10] The patient positioning and observation time is approximately 10–20 min.

Lumbar vertebrae have been characterized *in vitro* by ash mass, metrology, and bone densitometry techniques.[3,4] The directly measured quantities have been compared to the equivalent quantities determined *in vivo* by noninvasive techniques. The measured ash mass (mineral content excluding water, soft tissue, and other combustibles) is in the range 5–15 g. The ash mass is equivalent to the bone mineral content (BMC). The volume measured by metrology is in the range 30–50 cm^3, and this quantity may be determined by QCT techniques. The projected area measured by metrology is in the range 11–17 cm^2, depending on the viewing direction, and can be determined by radiographic projection techniques. The ash mass to volume values are in the range 0.20–0.35 g/cm^3, and this quantity is equivalent to the bone mineral volumetric density determined by QCT. The ash mass to projected area values are in the range 0.4–1.2 g/cm^2. This quantity is equivalent to the bone mineral areal density that is determined by most DEXA instruments, and this quantity is usually referred to as the bone mineral density (BMD).

DEXA instruments operated *in vivo* can typically determine the BMD to a precision of 2% or better. In addition, the absolute BMD, typically in the range 0.4–1.2 g/cm^2, can be determined to an accuracy of approximately 2%. The primary difficulty in the measurements is to account for the soft tissue areal density, along the same line of sight, with values up to 20–30 g/cm^2 in the case of the lumbar spine.

We have analyzed a newly developed pulsed x-ray source for the application to precision bone mineral densitometry. The x-ray fluence has dual-energy properties that, when enhanced by properly designed filtration, permits the implementation of dual-energy calibration and subtraction techniques. A computer model was developed for the simulation of the x-ray source, the filtration, the absorption by a bone/tissue object, and the dual-energy detection system. The analysis indicates that it is feasible to perform precision bone mineral densitometry, using a single x-ray pulse of 100 ns duration, for bone mineral and tissue densities that are characteristic of the lumbar spine and proximal femur. The precision is 2% over an area that is 15–20 mm in size, depending on the bone mineral and soft tissue thicknesses. A calibration algorithm was developed, based on a Plexiglas™/TiO_2 phantom, that results in a 2% uncertainty in the absolute BMD.

The clinical implementation of this flash x-ray absorptiometry (FXA) technique would have several attractive features. The BMD measurement is performed using a single short-duration x-ray pulse. The patient exposure time is minimal (100 ns), and this precludes the possibility of image blurring that would result from patient movement. Thus the patient immobilization time is also minimal. The precision and accuracy of the bone density measurements are expected to be comparable to existing DEXA units. The pulsed x-ray source is battery-powered and is portable, and this facilitates rapid BMD measurements in clinical and remote settings.

II. FLASH X-RAY SOURCE

A flash x-ray source has been developed and experimentally characterized.[12,13] The field emission x-ray tube, consisting of a tungsten anode and a mesh cathode in vacuum, is driven by a Marx generator. The operating characteristics were experimentally measured and compared to detailed computer simulations. Based on the simulations, the voltage and current characteristics and the x-ray flux were optimized for specific medical imaging applications.

The Marx generator, in its present configuration, is composed of 15 energy storage capacitors and 15 spark gap switches that are housed in an acrylic pressure vessel that is covered by a coaxial aluminum return-current cylinder. This design functions as a fast pulse forming line with low interstage inductance between the energy storage capacitors. The unit is 22 in. long, weights 26 lb, and is powered by a rechargeable battery. Approximately 100 x-ray exposures can be produced by a single battery charge.

The linear configuration of energy storage capacitors and spark gap switches can be easily altered for specific applications by adding additional capacitors. For the purpose of optimizing the capabilities of the x-ray source for dual-energy bone densitometry, the number of capacitors was increased from 15 to 30. The 30 capacitor generator produces a larger hard x-ray component that is desirable for dual-energy bone densitometry.

The equivalent circuits for the Marx generator and the x-ray tube are shown in Fig. 1. Indicated are the trigger circuit (stage 1), 29 identical circuits that contain an energy storage capacitor and a spark gap switch (stages 2–30), and

the x-ray tube circuit (stage 31). Each energy storage capacitor (C_1–C_{30}) has an associated inductance (L_1 or L_C) and a stray capacitance C_s to ground. Each spark gap switch has an inductance L_g and a resistance R_g. The x-ray tube is modeled by the inductance L_p and the resistance R_p that are associated with the peaking gap, and the inductance L_d and voltage V_d associated with the anode–cathode gap. The current and voltage across the anode–cathode gap are related by the Langmuir–Child law $i_{31}=PV_d^{3/2}$ where P is the perveance of the electron flow. The perveance was empirically determined by measuring the tube current and voltage of the 15 capacitor, 11 kV generator.[13]

The computer simulation of the Marx generator and the x-ray tube was based on the equivalent circuits shown in Fig. 1. An equation was written for each of the 31 stages:

$$(1/C_1+1/C_s)q_1+L_1(di_1/dt)$$
$$=q_2/C_s-(dC_1/dt)(V_0-q_1/C_1),$$

where $q=\int_0^1 i\,dt$,

$$(1/C_n+2/C_s)q_n+(L_g+L_c)(di_n/dt)+R_gi_n$$
$$=V_0+(q_{n-1}+q_{n+1})/C_s-(dC_n/dt)(V_0-q_n/C_n),$$

where $n=2$–30, and

$$q_{31}/C_s+(L_p+L_d)(di_{31}/dt)+R_pi_{31}=V_0-V_d+q_{30}/C_s.$$

The first equation represents the trigger circuit, the second equation the 29 identical circuits containing energy storage capacitors, and the last equation the x-ray tube circuit. These 31 time-dependent equations were solved for the currents by a fourth-order Runge–Kutta algorithm.

The various inductances that appear in the equations were calculated *ab initio* and had fixed values. The inductances were $L_1=24.15$ nH, $L_g=22.14$ nH, $L_C=1.37$ nH, $L_p=10.24$ nH, and $L_d=50$ nH. The capacitance of the energy storage capacitors was 8.325 nF. The stray capacitance was calculated to be $C_s=2.15$ pF. The effective resistance of the spark gap switches was determined by matching the damped oscillation of the current late in the pulse to the measured current for the 15 capacitor, 11 kV generator. The resistance values (R_g and R_p) were then set equal to 0.8 Ω.

The calculated x-ray tube current, voltage, and power are shown in Fig. 2. The initial electron acceleration phase is characterized by high tube perveance with a rapid increase in the tube current and voltage. This is followed by an arc phase in which the current continues to increase while the voltage and impedance across the tube rapidly collapse in the ensuing vacuum arc. The x-ray energy is relatively high early in the pulse (when the electron acceleration voltage is high) and decreases later in the pulse. The total charge delivered to the anode–cathode gap is 0.1 mA s.

The energy delivered to the anode–cathode gap, as a function of the electron acceleration voltage, was calculated from the time-dependent current and voltage. The energy distribution, in units of mJ per kV of anode–cathode gap voltage, is shown in Fig. 3(a). The energy delivered at the higher voltages (>150 kV) occurs primarily during the time of the current spike early in the current pulse when the voltage is maximal (see Fig. 2). The energy delivered at voltages of 30–150 kV occurs primarily during the middle of the current pulse when the current is high and the voltage is decreasing. This illustrates the dual-energy nature of the x-ray source, with harder x rays emitted during the initial charge-limited electron transport across the anode–cathode

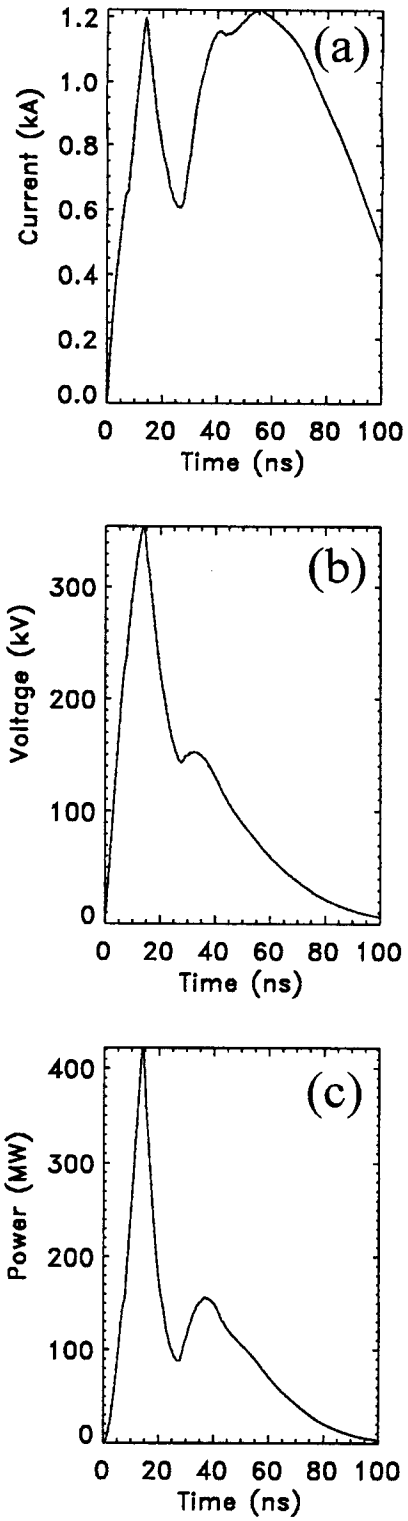

FIG. 2. (a) The x-ray tube current, (b) voltage, and (c) power.

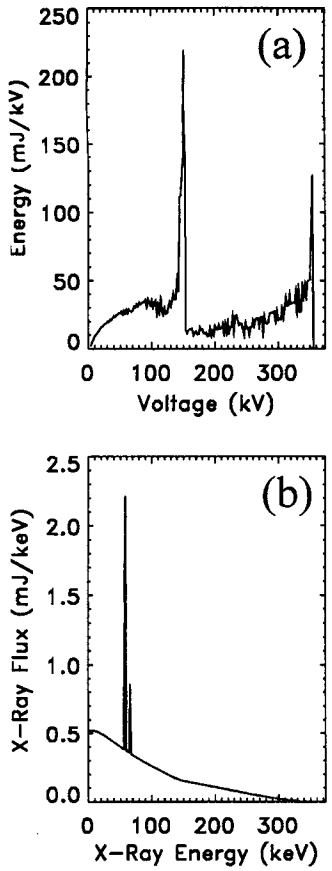

FIG. 3. (a) The energy delivered to the x-ray tube as a function of tube voltage, and (b) the x-ray energy distribution.

gap, and softer x rays emitted during the following arc phase of the discharge.

The x-ray energy distribution was calculated from the current and voltage by using a thick-target bremsstrahlung model and accounting for the tungsten K_α and K_β radiation.[14–16] The x-ray energy distribution, in units of mJ per keV of x-ray energy, is shown in Fig. 3(b). The discontinuity in the x-ray energy distribution near 150 keV results from the dual-energy nature of the energy distribution delivered to the x-ray tube. In effect, the discharge characteristics of the Marx generator and the anode–cathode load have been optimized to produce an enhanced high-energy x-ray component that is important for dual-energy densitometry.

The energy in the characteristic K_α and K_β x-ray lines is 4.7 mJ, and the energy in the continuum is 63 mJ. Of the 10 J energy that is initially stored in the energy storage capacitors, 9.8 J is delivered to the x-ray tube. The efficiency of conversion of the tube energy to x-ray energy is 0.7%.

III. DUAL-ENERGY X-RAY DISTRIBUTION

In general, a dual-energy x-ray distribution may be enhanced by switching the source voltage (developed by Hologic Inc.), changing the filtration (developed by Lunar Corp.), or a combination of these two techniques. Previous studies that were based on x-ray tube loading, x-ray quantum noise, and patient exposure established that x-ray energies in the two ranges 40–60 and 80–130 keV are suitable for dual-energy x-ray absorptiometry.[17,18] Most DEXA systems are limited by x-ray quantum noise, and other noise sources (such as phosphor, detector, and electronics) are smaller. Patient exposure is of primary concern and is usually lower than the exposure from other radiology procedures and from the natural background.

In our case, tube loading during a single x-ray pulse is minimal and is not a constraint on the design of the system. This permits the operation of the x-ray tube at higher voltage and power levels than is possible with more traditional x-ray tubes. The higher-energy x rays are of diagnostic importance because a higher x-ray fluence reaches the detector. Under some circumstances, this can result in an improved x-ray quantum signal to noise ratio and a reduced patient absorbed dose.

The x-ray detection system may also have energy-discrimination capabilities. Dual-energy detection systems are typically composed of a front panel or cassette that is sensitive to the soft x-ray component and a rear panel or cassette that is sensitive to the hard x-ray component. Energy discrimination may be enhanced by positioning an interdetector filter between the two panels to attenuate the residual soft x rays that may pass through the front panel. Dual-energy discrimination schemes were analyzed in Refs. 19–24 for chest radiography and mammography.

The contrast between soft tissue and bone is higher in the soft x-ray image and is lower in the hard x-ray image. The attenuation by soft tissue and bone may be inferred by analyzing the soft and hard x-ray images.[25–27] In addition, the exposure in the rear panel image by x rays scattered in the front panel may be substantially removed.[23]

In most analyses of DEXA systems, the signals are calculated using the attenuation coefficients of the filters and the object under study and the sensitivity of the detector. Scattered radiation is usually not considered for the design of the system. In any case, scattered radiation can be characterized and accounted for as part of the *in situ* calibration process.[23]

In this work, the computer model accounts for the energy-dependent attenuation of the x-ray fluence by the materials that are listed in Table I: The aluminum window of the x-ray tube, a tantalum prefilter that hardens the x-ray fluence and enhances the dual-energy distribution, a variable tissue areal density (0–30 g/cm^2), a variable bone mineral areal density (0–1.5 g/cm^2), a phosphor screen that is designed to absorb the soft x-ray component, an interdetector filter, and a scintillation fiber optic that absorbs the hard x-ray component. The material areal densities, volumetric densities, and thicknesses are listed in Table I. For each material, the energy-dependent attenuation coefficient was derived from the elemental compositions listed in Table I and the compilation of Ref. 28. The attenuation coefficient of tissue was assumed to be that of water. The bone mineral is hydroxyapatite ($Ca_5P_3O_{13}H$) with an assumed density of 0.25 g/cm^3 based on the lumbar vertebra metrology.

The x-ray fluence, in units of photons per keV per detector pixel, is shown in Fig. 4. For definiteness, we assume an x-ray source to object distance of 50 cm The detector is

TABLE I. The material compositions, densities, and thicknesses.

Material	Elemental composition	Density (g/cm^3)	Areal density (g/cm^2)	Thickness (mm)
Aluminum x-ray tube window	Al	2.7	0.054	0.2
Tantalum prefilter	Ta	16.6	0.17	0.1
Tissue (water)	H_2O	1.0	0–30	0–300
Bone mineral (hydroxyapatite)	$Ca_5P_3O_{13}H$	0.25	0–1.5	
Soft x-ray phosphor	Gd_2O_2S:Eu	7.5	0.15	0.2
Barium glass interdetector filter	SiO_2(Ba)	3.37	1.7	5
Hard x-ray scintillator	$SiO_2(Gd_2O_2S:Tb)$	5.0	7.5	15
Soft tissue phantom (Plexiglas)	$C_5H_8O_2$	1.19	0–30	0–252
Bone phantom (titanium dioxide)	TiO_2	4.05	0–1.5	0–3.7

placed directly behind the object. The detector resolution element is assumed to be of size 0.5 mm. The results may be geometrically scaled for a different source to object distance and detector resolution. Figure 4(a) shows the unfiltered x-ray fluence and Fig. 4(b) the fluence filtered by the 0.2-mm-thick aluminum vacuum window of the x-ray tube. An additional 0.1 mm tantalum prefilter hardens the fluence and enhances the dual-energy x-ray distribution, and the fluence after this filter is shown in Fig. 4(c). The soft x-ray band, at energies less than the tantalum K absorption edge at 69.5 keV, contains the tungsten K_α and K_β radiation near 58 and 67 keV, respectively. The hard x-ray band is maximal at 100 keV and extends to 300 keV.

For the purpose of determining the coefficient of variation of the BMD measurements, the x-ray fluence was calculated after passing through variable densities of soft tissue (0–30 g/cm^2) and bone mineral (0–1.5 g/cm^2). The x-ray fluence after passing through 20 g/cm^2 of soft tissue is shown in Fig. 4(d). The attenuation of the soft x-ray component is greater than that of the hard component. The x-ray fluence upon subsequently passing through 1.0 g/cm^2 of bone mineral is shown by the lower curve in Fig. 4(e), and the upper curve is the fluence for no bone thickness.

By comparing the two curves in Fig. 4(e), it is apparent that the energy distribution is considerably hardened by the attenuation of the soft x-ray component by bone mineral, and this is important for the sensitivity of the dual-energy technique for the precise determination of the BMD. In general, the soft x-ray energy component (40–70 keV) is designed to span the energy range where the attenuation of bone mineral (~1.0 g/cm^2) is rapidly decreasing with x-ray energy. The hard x-ray energy component is designed to penetrate the large soft tissue density (~20 g/cm^2).

The detector was assumed to be composed of a front phosphor screen that is optimized to absorb the soft x-ray component and a rear scintillator that absorbs the remaining hard x-ray component. The dual-energy discrimination is enhanced by an interdetector filter that preferentially attenuates the residual soft x rays that pass through the front phosphor screen. The phosphor was chosen to be Gd_2O_2S doped with Eu which fluoresces in the red region of the visible spectrum. The efficiency of conversion of x-ray energy to visible light energy is 15% (Levy Hill Laboratories Ltd., Cheshunt, United Kingdom). The K absorption edge of Gd is at 50.2

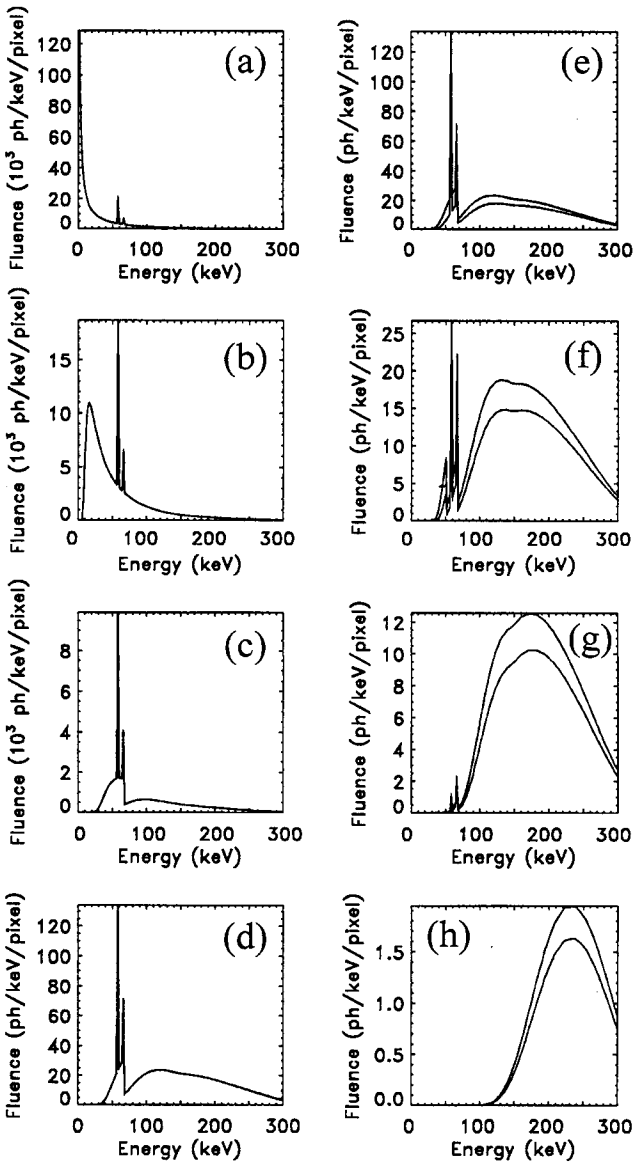

FIG. 4. (a) The unfiltered x-ray fluence, in units of 10^3 photons per keV per pixel, at a distance of 50 cm from the source and assuming a detector pixel of size 0.5 mm. The x-ray fluence after additional attenuation by (b) 0.2 mm aluminum, (c) 0.1 mm tantalum, (d) 20 cm tissue, (e) bone mineral, (f) 0.2 mm Gd_2O_2S:Eu, (g) 5 mm barium glass fiber optic, and (h) 15 mm scintillation fiber optic. The lower curves in (e)–(h) are for a 1.0 g/cm^2 BMD and the upper curves are for no BMD.

keV, and x rays with energies above this value, including the tungsten K radiation near 58 and 67 keV, are efficiently absorbed. The x-ray fluence after passing through a 0.2 mm thickness of the phosphor is shown in Fig. 4(f).

The interdetector filter was chosen to be a glass fiber optic plate with a high barium content (33% by weight; Schott Fiber Optics Inc., Southbridge, MA). The barium K absorption edge is at 37.4 keV, and the tungsten K radiation is strongly attenuated, as are x-ray energies up to about 100 keV. The x-ray fluence after passing through a 5 mm thickness of the barium glass is shown in Fig. 4(g), and this is the fluence that is incident on the scintillator. Thus the x-ray fluence that is absorbed by the scintillator is primarily the hard x-ray component with energies above 100 keV.

The scintillator was chosen to be a 15-mm-thick glass fiber optic plate doped with Gd_2O_2S:Tb (LG-9 plate; Schott Fiber Optics, Southbridge, MA). This material scintillates in the green region with an efficiency of 15%. Shown in Fig. 4(h) is the x-ray fluence after passing through the scintillator, which absorbs essentially all of the x-ray quanta with energies below 200 keV.

The x-ray fluences that are absorbed by the aluminum window, the tantalum prefilter, the object (tissue and bone mineral), and the detector components (phosphor, interdetector filter, and scintillator) are shown in Fig. 5. Of primary interest are the fluences absorbed by the front phosphor and the rear scintillator as shown in Figs. 5(e) and 5(g), respectively. The phosphor preferentially absorbs the soft x-ray component and the scintillator the hard component. This provides the basis for the dual-energy decomposition of the tissue and bone mineral attenuation.

For the purpose of determining the BMD, we assume that the red photons from the phosphor (the soft x-ray image) and the green photons from the scintillator (the hard x-ray image) are collected and separately detected. This may be accomplished by means of an imaging camera with multiple charge-coupled device (CCD) detectors that separately capture the red and green images (XC-003 RGB 3CCD camera, Sony Corp.). The computer model accounts for the transmission of the red photons through the phosphor and the channeling of the red photons through the barium glass and the scintillation fiber optic plates to the imaging system and the camera. The green photons are channeled through the scintillation fiber optic plate to the imaging system and the camera. We assume the collection efficiency of the imaging system is 10%.[29] We assume the detection efficiency of the camera system is 1%.

It will be shown that the number of visible light photons that are generated and detected is much greater than the number of x-ray quanta that are absorbed. Thus x-ray quantum noise is the dominant contributor to the coefficient of variation of the BMD.

An alternate means of separately detecting the optical photons generated by the soft and hard x-ray components is to use two tandem electronic detection panels that are in contact with the phosphor and the scintillator. This is analogous to using stacked film cassettes for multiple energy detection. The electronic detection panels may be of the amorphous silicon type that have been recently developed.[30] The active matrix of silicon pixels, each with a field effect transistor (FET), is fabricated on a thin glass substrate. Each pixel registers the charge resulting from the absorption of the optical photons. The panels are not susceptible to radiation damage. In this dual-energy x-ray detection scheme, the soft x-ray image is captured by the front phosphor/panel, and the hard x rays are transmitted to the rear scintillator/panel. The interdetector filter attenuates any soft x rays that may pass through the front phosphor/panel. Since the optical photons generated by the soft x-ray phosphor are captured by the front panel and are not channeled to another location for detection, it is not necessary that the interdetector filter and

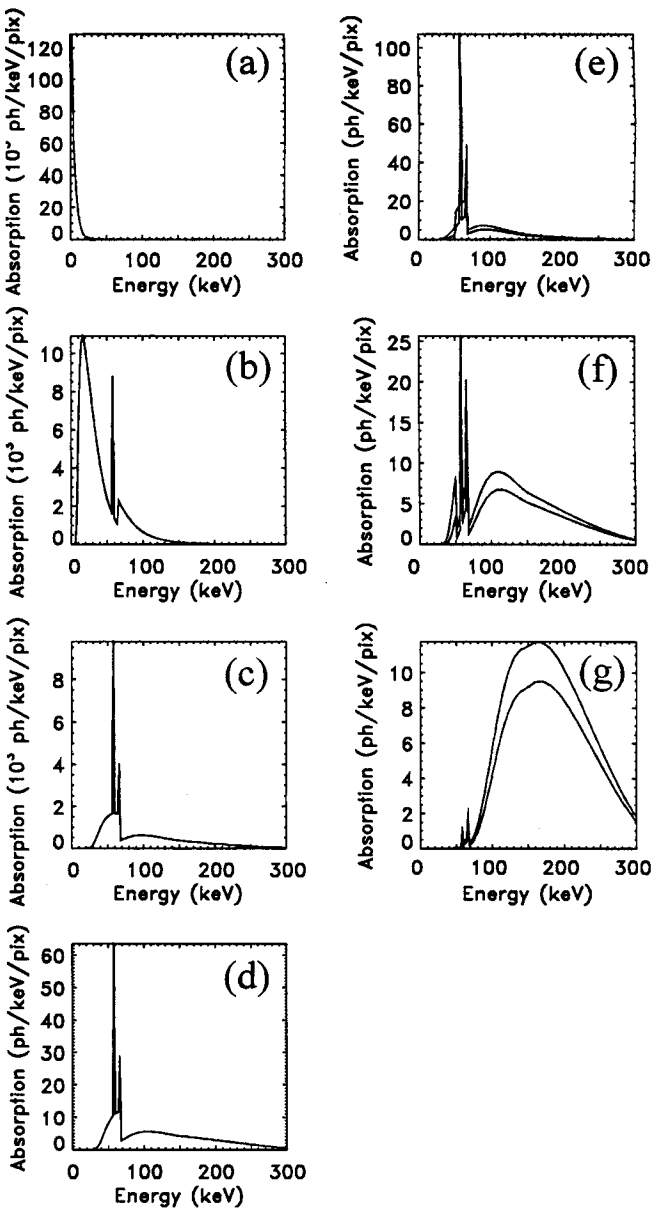

FIG. 5. The x-ray fluence absorbed per pixel by (a) 0.2 mm aluminum, (b) 0.1 mm tantalum, (c) 20 cm tissue, (d) 1.0 g/cm^2 bone mineral, (e) 0.2 mm Gd_2O_2S:Eu, (f) 5 mm barium glass fiber optic, and (g) 15 mm scintillation fiber optic. The lower curves in (e)–(g) are for a 1.0 g/cm^2 BMD, and the upper curves are for no BMD.

the hard x-ray scintillator be fiber optic plates. In addition, it is not necessary that the soft and hard x-ray conversion screens be of different types and generate optical photons of different colors.

A means of directly capturing the soft and hard x-ray images, without conversion to optical photons, is by use of two tandem amorphous silicon panels each with a photoconductive layer that converts the absorbed x-ray energy directly to charge.[31] The photoconductive material and the layer thickness may be chosen for the optimal conversion of the soft or hard x-ray component. Conversion layers consisting of amorphous Se, CdZnTe, and Pb_2I have been studied.

For definiteness, we assume the red phosphor and green scintillator dual-energy x-ray detection scheme. However, modeling indicates that the signals from the amorphous silicon panels would be comparable to those calculated for the red phosphor and green scintillator scheme.

IV. COEFFICIENT OF VARIATION

The coefficient of variation (CV) of the measurement of the BMD is calculated using the usual expressions[19]

$$\mathrm{CV}=(1/N_{\mathrm{pixels}}^{1/2})(\sigma(t_B)/t_B),$$

$$\sigma^2(t_B)=(\sigma^2(N_P)(\partial N_S/\partial t_T)_{t_B}^2+\sigma^2(N_S)\times(\partial N_P/\partial t_T)_{t_B}^2)J^{-2},$$

$$J=(\partial N_P/\partial t_T)_{t_B}(\partial N_S/\partial t_B)_{t_T}-(\partial N_S/\partial t_T)_{t_B}(\partial N_P/\partial t_B)_{t_T},$$

where t_B and t_T are the bone mineral and tissue areal densities, $\sigma(t_B)$ is the variance in the BMD measurement, N_{pixels} is the number of detector pixels in the region of interest, and N_P and N_S are the numbers of x-ray quanta absorbed per pixel in the phosphor and scintillator, respectively. The partial derivatives of N_P and N_S are taken at constant bone mineral or tissue densities. J is the Jacobian of the transformation from the densities (t_B and t_T) as a function of absorbed quanta (N_P and N_S) to the absorbed quanta as a function of densities. The latter quantities, the absorbed quanta as a function of the densities, are more convenient to calculate. We assume that $\sigma^2(N_P)=N_P$ and $\sigma^2(N_S)=N_S$.

The numbers of x-ray quanta (summed over energy) absorbed per pixel in the phosphor and the scintillator (N_P and N_S, respectively) are shown in Fig. 6(a) as functions of BMD and for a fixed tissue density of 20 g/cm^2. The numbers of absorbed x-ray quanta per pixel are approximately 600–900 for small BMD and decrease to 400–700 for 1.5 g/cm^2 BMD. The numbers of detected photons per pixel (red from the phosphor and green from the scintillator) are much larger and are shown in Fig. 6(e).

The CV is quite sensitive to the partial derivatives of the numbers of absorbed x-ray quanta per pixel that appear in the Jacobian. The slopes of the absorbed quanta curves as functions of bone mineral and tissue density are shown in Figs. 6(b) and 6(c). The slopes have large negative values for small densities, and this results in low CV values for small BMD.

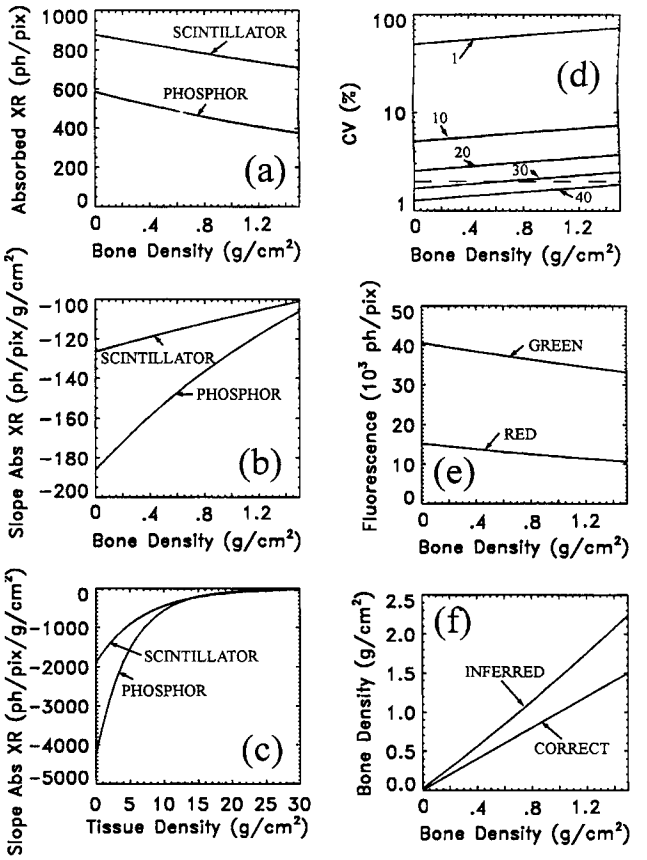

FIG. 6. (a) X-ray quanta absorbed per pixel in the phosphor and the scintillator for an assumed tissue density of 20 g/cm^2. The slope of the number of absorbed x rays (b) vs BMD for a fixed 20 g/cm^2 tissue density and (c) vs tissue density for a fixed 1.0 g/cm^2 BMD. (d) Coefficient of variation of the inferred BMD measurement. (e) Detected red and green photons per pixel. (f) Inferred and correct BMD. In (d)–(f), the assumed tissue density is 20 g/cm^2.

The CV values are shown in Fig. 6(d) for variable BMD and for a fixed tissue density of 20 g/cm^2. The curves are labeled by the pixel size of the square area (the region of interest) that was summed. For example, the curve labeled 30 is for summing over a 30×30 pixel area of size 15 mm (each pixel has an assumed size of 0.5 mm). The horizontal dashed line in Fig. 6(d) is the 2% CV level which is the goal for BMD measurements. Referring to Fig. 6(d), the CV is less than 2% for a 15 mm region of interest for BMD up to 0.6 g/cm^2 and for a 20 mm region of interest up to 1.5 g/cm^2. This spans the range of typical bone mineral densities of lumber vertebrae and the proximal femur.

V. DETERMINATION OF THE BONE MINERAL DENSITY

The value of the BMD can be inferred from the number of detected red and green photons from the phosphor and the scintillator shown in Fig. 6(e) and by using the average attenuation coefficients of tissue and bone mineral. Let τ_P and τ_S be the energy-averaged attenuation coefficients of tissue weighted by the number of x-ray quanta absorbed by the phosphor and the scintillator that are shown in Figs. 5(e) and

5(g), respectively. Let β_P and β_S be the energy-averaged attenuation coefficients of bone mineral weighted by the number of x-ray quanta absorbed by the phosphor and the scintillator, respectively. After passing through a tissue density of t_T and a BMD of t_B, the x rays that are absorbed by the phosphor and the scintillator result in red and green photon fluences of

$$R = R_0 e^{-\tau_P t_T - \beta_P t_B} \quad G = G_0 e^{-\tau_S t_T - \beta_S t_B},$$

where R_0 and G_0 are the red and green fluences in the absence of the bone and tissue materials. The tissue density t_T can be eliminated, and the two equations can be solved for the BMD,

$$t_B = (\rho \ln(G_0/G) - \ln(R_0/R))/\delta,$$

where $\rho = \tau_P/\tau_S$ and $\delta = \rho\beta_S - \beta_P$. In effect, the soft tissue contribution has been removed from the hard x-ray signal.

The inferred BMD is shown by the upper curve in Fig. 6(f) for the case of a fixed tissue density of 20 g/cm^2, and the lower curve is the correct BMD. The inferred BMD is inaccurate at larger values of BMD, and this indicates the need for a calibration phantom as discussed in Sec. VI.

Contour plots of the number of x rays absorbed by the phosphor and the scintillator, in units of 10^3 quanta per pixel, are shown in Figs. 7(a) and 7(b). These data are plotted as functions of the tissue and bone mineral densities in units of g/cm^2. The corresponding number of detected red and green photons, in units of 10^3 photons per pixel, are shown in Figs. 7(c) and 7(d). It is apparent that the x-ray quantum noise is higher than the visible photon noise throughout the range of tissue and bone densities.

The CV for regions of interest of sizes 10 and 20 mm are shown in Figs. 7(e) and 7(f), respectively. For a 20 mm region of interest, the CV values are less than 2% for the range of BMD that is typically encountered in lumbar spine and proximal femur densitometry.

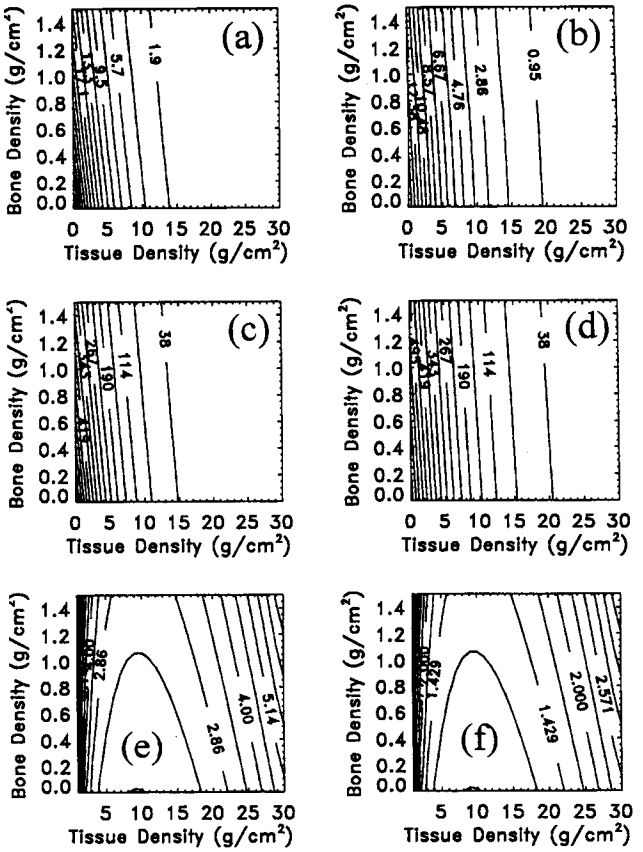

FIG. 7. The number of x-ray quanta absorbed per pixel in (a) the phosphor and (b) the scintillator in units of 10^3 quanta. The number of (c) red and (d) green photons detected per pixel in units of 10^3 photons. The coefficient of variation of the BMD measurement for a region of interest of size (e) 10 mm and (f) 20 mm.

VI. CALIBRATION PHANTOM

In order to improve the accuracy of the inferred BMD, a calibration phantom was implemented in the computer model. Traditional calibration phantoms are commonly composed of Plexiglas to simulate soft tissue and aluminum to simulate bone mineral. As listed in Table I, Plexiglas has a composition $C_5H_8O_2$ and a density 1.19 g/cm^3. The x-ray attenuation of Plexiglas is similar to that of soft tissue.[32]

The atomic number (13) of aluminum is similar to the weight-averaged atomic number (14.1) of hydroxyapatite ($Ca_5P_3O_{13}H$), the major constituent of bone mineral. However, the attenuation coefficients of aluminum and hydroxyapatite significantly differ at the soft and hard x-ray energies typically used for dual-energy bone densitometry. A search of readily available materials revealed that TiO_2 is a better calibration phantom for hydroxyapatite than is aluminum. For an appropriate thickness of TiO_2, the attenuation coefficients at the soft and hard x-ray energies are in good agreement with those of hydoxyapatite.

The attenuation coefficients of tissue and bone mineral were replace by those of Plexiglas and TiO_2 in the computer model. The same procedure was used to calculate the x rays absorbed in the phosphor and scintillator and the resulting detected red and green photons. The calibration quantities ρ and δ were derived for the calibration phantom.

The ratio of the ρ values for the tissue/bone case and the Plexiglas™/TiO_2 case is shown in Fig. 8(a). The corresponding ratio of the δ values is shown in Fig. 8(b). These ratios were used to correct the ρ and δ values that were used to calculate the BMD. This was done by fitting a smooth surface, that was a polynomial function of the tissue and bone mineral densities, to the surfaces shown in Figs. 8(a) and 8(b).

Shown in Figs. 8(c) and 8(d) are the derived BMD and the percent error in the BMD, respectively, for the case of a first-order (linear) polynomial fit to the surfaces of Figs. 8(a) and 8(b). The corresponding cases of a second-order (quadratic) polynomial fit and a third-order (cubic) polynomial fit are shown in Figs. 8(e)–8(h). The errors in the inferred BMD are less than 2% for the quadratic and cubic fits except for very small values of bone mineral and tissue densities. Thus a reasonably low-order polynomial correction can be made

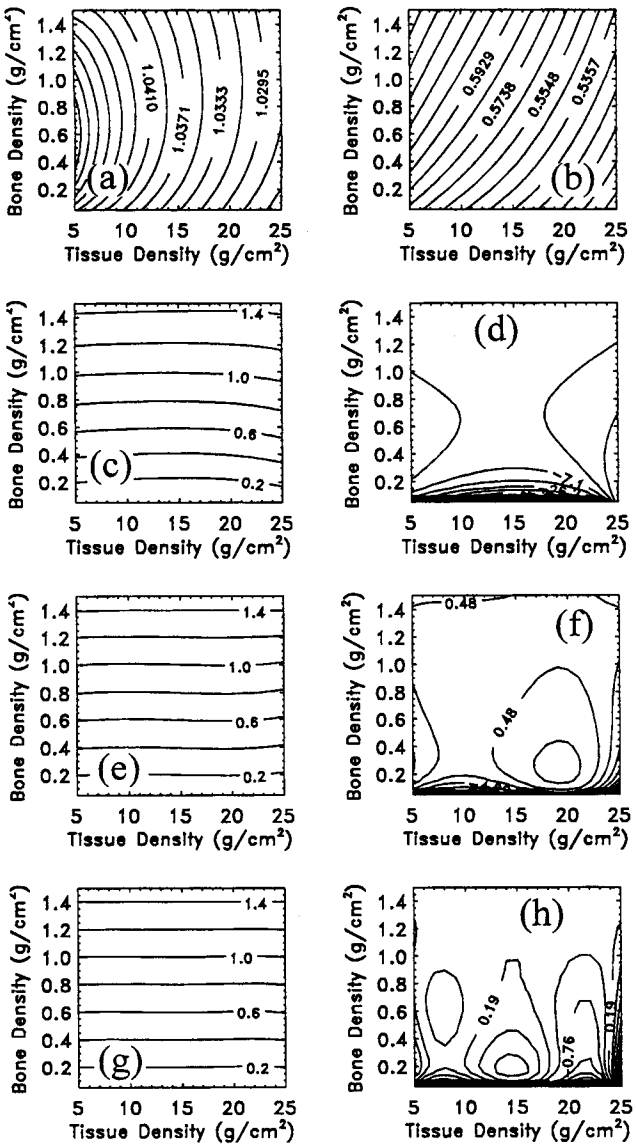

FIG. 8. The ratio of the tissue/bone and Plexiglas™/TiO_2 decomposition values (a) ρ and (b) δ. (c) The inferred BMD and (d) the percent error in the BMD for the case of a first-order polynomial fit to the decomposition ratio values. (e) The inferred BMD and (f) the percent error for the case of a second-order polynomial fit to the decomposition ratio values. (g) The inferred BMD and (h) the percent error for the case of a third-order polynomial fit.

to the inferred bone density by using the Plexiglas™/TiO_2 calibration phantom.

VII. X-RAY EXPOSURE AND ABSORBED DOSE

The x-ray exposure was determined by calculating the energy-dependent ionization of air using the technique of Ref. 33. The exposure after the x-ray fluence had been attenuated by the tantalum prefilter was calculated. This was the fluence that was incident on the tissue/bone object. The exposure resulting from the soft x-ray component, summed over x-ray energies of 0–70 keV, was 1.8 mR, where 1 mR is equivalent to an ionization charge of 2.58×10^{-4} C per 1 g of dry air. The exposure resulting from the hard x-ray component (>70 keV) was 1.9 mR. The total patient exposure, at a distance of 50 cm from the x-ray source, was therefore 3.7 mR.

The average x ray dose that was absorbed by 20 cm of tissue was calculated from the tissue absorption curve shown in Fig. 5(c). The absorbed dose was 2.4 and 1.9 mrem in the low and high x-ray energy components, respectively. The total absorbed dose was therefore 4.3 mrem.

After attenuation by 20 cm of tissue, the average x-ray dose absorbed by a BMD of 1.0 g/cm^2 was calculated using the bone mineral absorption curve of Fig. 5(d). The absorbed dose was 0.27 and 0.35 mrem in the soft and hard x-ray components, respectively, and the total dose was 0.62 mrem. Thus the soft x-ray component contributes the major part of the average absorbed tissue dose, and the hard x-ray component contributes the major part of the average absorbed BMD dose.

VIII. SUMMARY

Based on computer modeling, the feasibility of using a newly developed pulsed x-ray source for precision bone mineral densitometry has been analyzed. The x-ray source is portable and battery powered, and these are attractive features for rapid BMD measurements in clinical and remote situations.

The BMD measurement is performed using one x-ray pulse of 100 ns duration. The x-ray fluence has dual-energy properties, and the dual-energy distribution is enhanced by use of a tantalum prefilter. At a distance of 50 cm from the source, the patient exposure is 3.7 mR. The average absorbed dose for a tissue density of 20 g/cm^2 and a BMD of 1 g/cm^2 is 4.3 and 0.62 mrem, respectively.

The soft and hard x-ray images are recorded by a detection system with dual-energy discrimination properties. In the detection system that is considered, the soft x rays are preferentially absorbed by a red emitting Gd_2O_2S:Eu phosphor. The hard x rays are absorbed by a Gd_2O_2S:Tb scintillation fiber optic plate that fluoresces at green wavelengths. Using a dual-energy decomposition technique, the soft tissue contribution is removed, and the BMD is determined.

The precision of the measured BMD is 2% for a region of interest of size 15–20 mm, depending on the assumed tissue and bone mineral densities. The ranges of tissue and bone mineral densities that were studied are characteristic of the lumbar spine and the proximal femur. An algorithm was developed for using a Plexiglas™/TiO_2 calibration phantom to achieve 2% absolute accuracy in the inferred BMD.

This analysis indicates that it may be feasible to perform precision BMD measurements using a flash x-ray absorptiometry (FXA) technique. A more extensive system design study is needed to minimize the patient dose and to optimize the precision of the BMD measurements of specific anatomical sites. Alternative dual-energy detection schemes, such as direct or indirect x-ray detection by amorphous silicon panels, should be studied in detail. Additional analysis is also needed to assess the effect of x-ray scattering on the measurement of the BMD.

ACKNOWLEDGMENT

This work was supported by the Office of Naval Research.

[a]Electronic mail: john.seely@nrl.navy.mil

[1]H. K. Genant, K. Engelke, T. Fuerst, C. Glüer, S. Grampp, S. Harris, M. Jergas, T. Lang, Y. Lu, S. Majumdar, A. Mathur, and M. Takada, "Non-invasive assessment of bone mineral and structure: State of the art," J. Bone Min. Res. **11**, 707–730 (1996).

[2]R. W. Lymn and S. L. Gordon, "The effects of space travel on the musculoskeletal system," National Institutes of Health, Publication No. 93–3484 (1992).

[3]C. P. Ho, R. W. Kim, M. B. Schaffler, and D. J. Sartoris, "Accuracy of dual-energy radiographic absorptiometry of the lumbar spine: Cadaver study," Radiology **176**, 171–173 (1990).

[4]J. S. Finkelstein, R. Cleary, J. Butler, R. Antonelli, B. Mitlak, D. Deraska, J. Zamora-Quezada, and R. Neer, "A comparison of lateral versus anterior-posterior spine dual energy x-ray absorptiometry for the diagnosis of osteopenia," J. Clin. Endocrinology Metabolism **78**, 724–730 (1994).

[5]M. Jergas, M. Breitenseher, C. Glüer, W. Yu, and H. Genant, "Estimates of volumetric bone density from projectional measurements improve the discriminatory capability of dual x-ray absorptiometry," J. Bone Min. Res. **10**, 1101–1110 (1995).

[6]M. Takada, S. Grampp, X. Ouyang, K. Engelke, and H. Genant, "A new trabecular region of interest for femoral dual x-ray absorptiometry: Short-term precision, age-related bone loss, and fracture discrimination compared with current femoral regions of interest," J. Bone Min. Res. **12**, 832–838 (1997).

[7]X. G. Cheng, P. Nicholson, S. Boonen, G. Lowet, P. Brys, J. Aerssens, G. van der Perre, and J. Dequeker, "Prediction of vertebral strength *in vitro* by spinal bone densitometry and calcaneal ultrasound," J. Bone Min. Res. **12**, 1721–1728 (1997).

[8]T. V. Nguyen, P. Sambrook, and J. Eisman, "Sources of variability in bone mineral density measurements: Implications for study design and analysis of bone loss," J. Bone Min. Res. **12**, 124–135 (1997).

[9]T. Lang, M. Takada, R. Gce, C. Wu, J. Li, C. Hayashi-Clark, S. Schocn, V. March, and H. Genant, "A preliminary evaluation of the Lunar Expert-XL for bone densitometry and vertebral morphometry," J. Bone Min. Res. **12**, 136–143 (1997).

[10]H. K. Genant, S. Grampp, C. C. Glüer, K. G. Faulkner, M. Jergas, K. Engelke, S. Hagiwara, and C. van Kuijk, "Universal standardization for dual x-ray absorptiometry: Patient and phantom cross-calibration results," J. Bone Min. Res. **9**, 1503–1514 (1994).

[11]N. A. Pocock, K. Noakes, M. Griffiths, N. Bhalerao, P. Sambrook, J. Eisman, and J. Freund, "A comparison of longitudinal measurements in the spine and proximal femur using Lunar and Hologic instruments," J. Bone Min. Res. **12**, 2113–2118 (1997).

[12]C. N. Boyer, G. E. Holland, and J. F. Seely, "A pulsed hard x-ray source for nondestructive testing and medical imaging," Proc. SPIE **3154**, 16 ().

[13]C. N. Boyer, G. E. Holland, and J. F. Seely, "Portable hard x-ray source for nondestructive testing and medical imaging," Rev. Sci. Instrum. **69**, 2524–2530 (1998).

[14]M. Green and V. E. Cosslett, "The efficiency of production of characteristic x-radiation in thick targets of a pure element," Proc. Phys. Soc. London **78**, 1206–1214 (1961).

[15]P. Tothill, "The ratio of K characteristic to total radiation emitted from a tungsten target x-ray tube," Br. J. Appl. Phys., J. Phys. D **1**, 1093–1107 (1968).

[16]R. Birch and M. Marshall, "Computation of bremsstrahlung x-ray spectra and comparison with spectra measured with Ge(Li) detector," Phys. Med. Biol. **24**, 505–517 (1979).

[17]J. A. Sorenson, P. Duke, and S. Smith, "Simulation studies of dual-energy x-ray absorptiometry," Med. Phys. **16**, 75–80 (1989).

[18]D. P. Chakraborty and G. T. Barnes, "Bone mineral densitometry with x-ray and radionuclide sources: A theoretical comparison," Med. Phys. **18**, 978–984 (1991).

[19]G. T. Barnes, R. Sones, M. Tesic, D. Morgan, and J. Sanders, "Detector for dual-energy digital radiography," Radiology **156**, 537–540 (1985).

[20]D. P. Chakraborty and G. T. Barnes, "An energy sensitive cassette for dual-energy mammography," Med. Phys. **16**, 7–13 (1989).

[21]J.-T. Ho, R. A. Kruger, and J. A. Sorenson, "Comparison of dual and single exposure techniques in dual-energy chest radiography," Med. Phys. **16**, 202–208 (1989).

[22]J. M. Boone, G. Shaber, and M. Tecotzky, "Dual-energy mammography: A detector analysis," Med. Phys. **17**, 665–675 (1990).

[23]D. L. Ergun, C. Mistretta, D. Brown, R. Bystrianyk, W. Sze, F. Kelcz, and D. Naidich, "Single-exposure dual-energy computed radiography: Improved detection and processing," Radiology **174**, 243–249 (1990).

[24]R. E. Alvarez, "Active energy selective image detector for dual-energy computed radiography," Med. Phys. **23**, 1739–1748 (1996).

[25]R. Alvarez and E. Seppi, "A comparison of noise and dose in conventional and energy selective computed tomography," IEEE Trans. Nucl. Sci. **NS-26**, 2853–2856 (1979).

[26]L. A. Lehmann, R. Alvarez, A. Macovski, and W. Brody, "Generalized image combinations in dual KVP digital radiography," Med. Phys. **8**, 659–667 (1981).

[27]B. K. Stewart and H. K. Huang, "Single-exposure dual-energy computed radiography," Med. Phys. **17**, 866–875 (1990).

[28]C. T. Chantler, "Theoretical form factor, attenuation and scattering tabulation for $Z=1-92$ from $E=1-10$ eV to $E=0.4-1.0$ MeV," J. Phys. Chem. Ref. Data **24**, 71 (1995).

[29]S. Hejazi and D. Trauernicht, "System considerations in CCD-based x-ray imaging for digital chest radiography and digital mammography," Med. Phys. **24**, 287–297 (1997).

[30]L. E. Antonuk, Y. El-Mohri, J. Siewerdsen, J. Yorkston, W. Huang, V. Scarpine, and R. Street, "Empirical investigation of the signal performance of a high-resolution, indirect detection, active matrix flat-panel imager (AMFPI) for fluoroscopic and radiographic operation," Med. Phys. **24**, 51–70 (1997).

[31]W. Zhao and J. A. Rowlands, "Digital radiology using active matrix readout of amorphous selenium: Theoretical analysis of detective quantum efficiency," Med. Phys. **24**, 1819–1833 (1997).

[32]E. C. McCullough, "Photon attenuation in computed tomography," Med. Phys. **2**, 307–320 (1975).

[33]J. D. Cox, D. W. Williams, and D. S. Langford, "Direct x-ray sensing CCD array for intraoral dental x-ray imaging system," Proc. SPIE **2163**, 284–297 (1994).